ACS OMEGA

http://pubs.acs.org/journal/acsodf
Article

Combined Charge Extraction by Linearly Increasing Voltage and Time-Resolved Microwave Conductivity to Reveal the Dynamic Charge Carrier Mobilities in Thin-Film Organic Solar Cells

Shaoxian Li, Ryosuke Nishikubo, and Akinori Saeki*

Cite This: ACS Omega 2024, 9, 26951−26962
Read Online

ABSTRACT: This article reports a purely experiment-based method to evaluate the time-dependent charge carrier mobilities in thin-film organic solar cells (OSCs) using simultaneous charge extraction by linearly increasing the voltage (CELIV) and time-resolved microwave conductivity (TRMC) measurements. This method enables the separate measurement of electron mobility (μ_e) and hole mobility (μ_h) in a metal−insulator-semiconductor (MIS) device. A slope-injection-restoration voltage profile for MIS-CELIV is also proposed to accurately determine the charge densities. The dynamic behavior of μ_e and μ_h is examined in five bulk heterojunction (BHJ) OSCs of polymer:fullerene (P3HT:PCBM and PffBT4T:PCBM) and polymer:nonfullerene acceptor (PM6:ITIC, PM6:IT4F, and PM6:Y6). While the former exhibits fast decays of μ_h and μ_e, the latter, in particular, PM6:IT4F and PM6:Y6, exhibits slow decays. Notably, the high-performing PM6:Y6 demonstrates both a balanced mobility (μ_e/μ_h) of 1.0−1.1 within 30 μs and relatively large CELIV-TRMC mobility values among the five BHJs. The results exhibit reasonable consistency with a high fill factor. The proposed new CELIV-TRMC technique offers a path toward a comprehensive understanding of dynamic mobility and its correlation with the OSC performance.

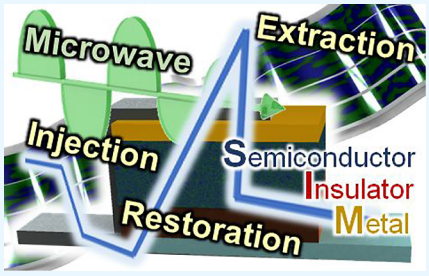

1. INTRODUCTION

The power conversion efficiency (PCE) of bulk heterojunction (BHJ) organic solar cells (OSCs) has improved dramatically over the past 20 years, approaching 20%.[1−3] Nonfullerene acceptor (NFA) OSCs[4−7] have led the PCE record for years; however, the reason for their high performance is still not fully understood, especially from the charge transport perspective.[8−11] The charge transport of OSCs is usually characterized by the charge carrier mobility (μ), which plays a vital role in charge separation,[12] recombination,[13] and extraction,[14] and is thus considered to significantly affect OSC performance.[10,15] Additionally, a well-balanced electron/hole mobility is important as it prevents the space-charge effect.[16] However, even when both the mobility value and balance are considered, many OSC studies fail to account for their performance differences. For example, it is unclear why space-charge limited current (SCLC) measurements of PM6:BTP-eC9 processed from chlorobenzene (CB) yield a higher electron mobility (μ_e = ∼4.0 × 10^{-4} cm^2 V^{-1} s^{-1}) and balanced mobility (μ_h/μ_e ∼ 1.8), as compared with that processed from chloroform (CF; μ_e = ∼2.3 × 10^{-4} cm^2 V^{-1} s^{-1}); however, the latter exhibits a higher fill factor (FF, ∼0.74) than the former (∼0.68).[17] One possible reason for these inconsistencies is the accuracy of the mobility measurements.[18]

Conventionally, charge mobility is regarded as a space- and time-independent constant during charge transport in OSCs and is usually measured using techniques such as SCLC,[19] time-of-flight (TOF),[20] field-effect transistors,[21] and charge extraction by linearly increasing voltage (CELIV).[22−24] These measurements are direct and easy to implement, but they provide only a long-range and averaged mobility value. Empowered by time-resolved techniques, such as electric field-induced second harmonic,[12,25] time-resolved terahertz spectroscopy,[26] and time-resolved microwave conductivity (TRMC),[18,27−34] the mobility of charge carriers has recently been observed to decay during charge transport (termed mobility relaxation) after photo injection. Melianas et al. reported that the charge mobility in OSCs exhibits a very large initial mobility (>1 cm^2 V^{-1} s^{-1}), which gradually decreases (by as large as 6 orders of magnitude) because the charge carrier transports to the electrode via hopping between the tail states in the density of states.[18] Time-dependent mobility also helps explain the measurement technique dependence of charge mobility (for example, the TRMC mobility is generally 2 to 3 orders of magnitude larger than that of CELIV)[18,32,36,37] because each technique has its characteristic time scale.

We previously reported a combination of TRMC and TOF measurements to determine the time-dependent electron/hole mobilities in various BHJ OSCs.[34] Very distinct mobility

Received: December 13, 2023
Revised: May 22, 2024
Accepted: June 5, 2024
Published: June 13, 2024

https://doi.org/10.1021/acsomega.3c09977
ACS Omega 2024, 9, 26951−26962

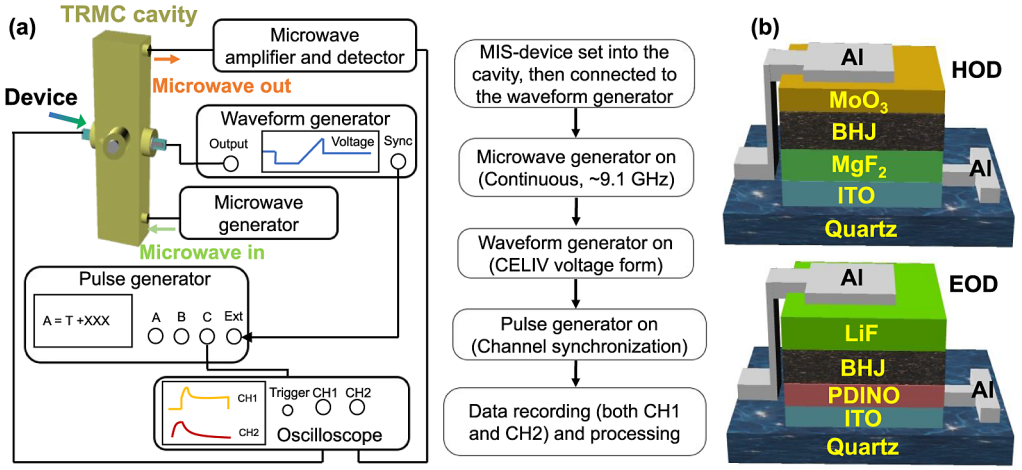

Figure 1. (a) Schematics of the CELIV-TRMC measurement system (left) and experimental procedures (right). (b) Device structures of an HOD (upper image, 50 nm-thick MgF_2 was used as an insulator) and an EOD (bottom image, 100 nm-thick LiF was used as an insulator).

relaxation characteristics in the fullerene-based OSCs (PCPDTBT:PC_{71}BM and PffBT4T:PC_{61}BM)[31,34] and NFA OSCs (PBDB-T:PC_{61}BM and PBDB-T:ITIC)[28] were revealed, with the mobility relaxation lifetimes differing by as much as 2 orders of magnitude. However, the TOF-TRMC measurement exhibits drawbacks, namely, (i) only the normalized mobility is derived; (ii) the mobility determination includes a diffusion-based simulation, which may result in a deviation in the analyzed mobility; and (iii) most importantly, the photoactive layer thickness of a TOF-TRMC device is 1−2 μm (5−10-fold thicker than real OSCs) owing to the TOF limitation,[35] which may lead to morphological differences. Therefore, an alternative to the TOF measurements is desirable.

To address this issue, TRMC and CELIV measurements were combined to determine the time-dependent electron−hole mobilities in a series of OSCs. Photo- and dark-CELIVs have often been used to evaluate charge carrier mobility, the active layer thickness of which is identical to those of real OSC devices.[36−40] Genevičius et al. measured the time-dependent photo-CELIV mobilities in regiorandom poly(3-hexylthiophene), obtaining values of 10^{-6}−10^{-5} cm^2 V^{-1} s^{-1} at time scale of 1−7 ms through controlling the delay time.[40] However, such mobilities include contributions from both electrons and holes, while they cannot be separated. On the other hand, a metal−insulator-semiconductor (MIS) device for CELIV can separately evaluate μ_h and μ_e in a hole-only device (HOD) and electron-only device (EOD), respectively. However, only time-averaged mobility can be obtained, which is usually based on an assumed charge carrier distribution, a material-conductivity-dependent correlation factor, and a drift-dominated transport model.[41,42] Our dark TRMC-CELIV in an MIS device provides a method to simultaneously evaluate the time-dependent TRMC transient conductivity, injected charge density, and CELIV mobility. For this purpose, the authors also proposed a slope-injection-restoration voltage that allows for an accurate determination of the charge density. The time-dependent μ_h and μ_e at a real OSC thickness were investigated purely based on experimental parameters. Two conventional polymers, namely, fullerenes (P3HT:PC_{61}BM, PCE ∼ 4%; PffBT4T:PC_{61}BM, PCE ∼ 9%)[33] and three well-performing polymers, NFAs (PM6:ITIC, PCE ∼ 10%;[4] PM6:IT4F, PCE ∼ 13%;[1] and PM6:Y6, PCE ∼ 16%),[43] were selected as BHJ materials. These BHJs presented distinct mobility decay characteristics, and a comparison of these results provided important insights into the origin of the high FF and PCE of PM6:Y6.

2. RESULTS AND DISCUSSION

2.1. Calibration of the TRMC Sensitivity Factor to Determine Δσ. Figure 1a schematically illustrates the CELIV-TRMC measurement system. The fabricated MIS device (Figure 1b) was set in a harmonic transmission-type resonant cavity (TE_{10m}, m = 14), where the TRMC signals were probed by continuous microwaves (∼9.16 GHz, ∼50 mW) generated by using a microwave signal generator. The change in the TRMC transient conductivity ($\Delta\sigma$) is related to the charge carrier mobility (μ), as detailed in eq 1.[44−47]

$$\Delta\sigma = e\Delta(n\mu) = \frac{1}{A}\cdot\frac{\Delta P}{P} \quad (1)$$

where e is the elementary charge, n is the charge carrier density, A is the sensitivity factor, ΔP is the change in microwave power, and P is the incident microwave power. A of a resonant cavity is well formulated and depends on the quality factor of the microwave cavity (Q), ratio of incident and reflected microwave power, resonant frequency (f_0), and measured sample geometry. Owing to the high microwave reflection and absorption of the electrodes in our MIS-CELIV device, a transmission-type microwave cavity was used instead of a conventional reflection-type resonant cavity (otherwise no resonant frequency could be found). However, the formula for determining the A value for a transmission-type microwave cavity has not yet been reported. Thus, a comparison based on flash-photolysis TRMC technique was used to determine the A for our transmission-type cavity, in which a sample was subsequently measured with a reflection-type cavity to determine $\Delta\sigma$ (formula proposed by Warman et al.[45] and a transmission type cavity to determine $\Delta P_t/P_t$ (P_t is the transmitted microwave power), both under the same laser irradiation (λ = 532 nm) to yield the same $\Delta\sigma$. The A value was then calculated by $\Delta P_t/P_t/\Delta\sigma$. The $\Delta\sigma$ and $\Delta P_t/P_t$ of an identical BHJ/quartz sample were first compared (Figure S1), rendering an A of 100−140 m/S at P_i = 16.5 dBm (here A is insignificantly dependent on the laser intensity while negatively dependent on P_i). Furthermore, by considering that A is proportional to Q and that Q is 3200 for a BHJ/quartz sample

https://doi.org/10.1021/acsomega.3c09977
ACS Omega 2024, 9, 26951−26962

and 450 for an MIS-CELIV sample in a transmission cavity (Figure S2a−c), A is roughly estimated to be ∼20 m S^{-1}.

For a more direct and precise determination of A, we adopted the $(FAPbI_3)_{0.87}(MAPbBr_3)_{0.13}$ perovskite (fabricated according to ref 48 as the photoactive layer due to the large reported TRMC mobility of >10 cm^2 V^{-1} s^{-1} (over 3 orders larger than that of our BHJ materials),[49] rendering a large $\Delta P_t/P_t$ signal of the MIS-CELIV device. The Q values of perovskite/quartz and MIS-CELIV (perovskite) samples are 3200 and 470 (Figure S2d,e), respectively, almost identical to those of the BHJ samples. Through comparing the $\Delta\sigma$ of a perovskite/quartz sample to the $\Delta P_t/P_t$ of a perovskite/quartz sample (Figure S3a) or to that of a MIS-CELIV (perovskite) sample (Figure S3b), the calculated A values of MIS-CELIV (perovskite) and perovskite/quartz samples at various P_i are shown in Figure S3c. The $\Delta\sigma$ and $\Delta P_t/P_t$ of a perovskite/quartz sample showed a good fit with A ∼ 150 m S^{-1} (very close to that of BHJ/quartz sample, ∼100−140 m S^{-1}), which suggests A is negligibly dependent on the active layer materials. The light intensity dependence of A was also investigated (Figure S3d), while within the excitation photon flux range (10^{14}−10^{16} photons cm^{-2} s^{-1}), the A was insignificantly dependent on the carrier density. Thus, A of 13 m S^{-1} was obtained at a set P_i = 16.5 dBm for our MIS-CELIV device in a transmission-type cavity (f_0 = 9.16 GHz), which is 3 to 4 orders of magnitude smaller than that of a resonant cavity.[49] Because the A value depends on the thickness of the Al electrode and the resistance of the indium tin oxide (ITO) layer, the electrode geometry of all of the devices was controlled to be the same.

2.2. Modified Injection Voltage Profile of CELIV and Analysis Method. Figure 2 shows schematics of the CELIV voltage profile and typical transient current (I). The areas of the yellow-filled regions represent the injected charge amount (Q_{inj}) and extracted charge amount (Q_{ext}), which can be determined using eq 2:

$$Q_{inj} \text{ or } Q_{ext} = \int_{t_0}^{t_1} |I(t) - I_0 - I_{ohm}(t)| d\,t \quad (2)$$

where $I(t)$ is the measured CELIV current transient, I_0 is the current plateau during charge injection and extraction relevant to Q_{inj} and Q_{ext}, respectively, and t_0 and t_1 are the beginning and ending points of an injection or extraction process, respectively.[51] In this paper, t_0 is defined as the time point when the current first reaches I_0, which is to minimize the effect of device RC[52,53] (∼3 μs as roughly estimated in Figure S10a) and the difference between applied injection voltage and the build-in voltage of MIS device (see Supporting Note S1 for detailed discussion).[54,55] Moreover, in the case of charge extraction, t_0 does not necessarily equal the real start point of charge extraction in our MIS-CELIV device because the accumulated charge carriers near the insulator/semiconductor interface need a certain time to reach the counter electrode. Nevertheless, from the change of TRMC signals near t_0 point (Figure S5) and the mobility decay feature of the device (vide infra), t_0 is considered close to the time point when the injected carriers start to leave the device (schematic shown in Figure S7b). The reason is as follows: first, based on the deviation point of the extraction current curves with/without charge carriers (Figure S6b, an extraction without carriers yields only a capacitive current), the injected carriers start to move toward the electrode prior to t_0 (though they do not necessarily reach the electrode); second, if t_0 locates far prior to the start point of carriers leaving the device, then the mobility decay during carrier motion should result in a significant TRMC decay. However, since no obvious TRMC decay was observed near t_0 (Figure S5b), t_0 is considered to locate near the starting point of carriers leaving the device. Furthermore, by calculating the charges between t_{ext} (the start point of extraction voltage ramp, see Figure S6b) and the transit time[38] of surface charge distribution and comparing the results with the total extractable charge (Figure S7a), the resultant error in calculated Q_{ext} (and the estimated time-dependent mobility, vide infra) is <10% (see Supporting Note S1 and Figures S4−S7 for detailed discussion). Therefore, our determination of t_0 is considered feasible and accurate. This study introduces a new factor (I_{ohm}) to calibrate the current proportion associated with the common ohmic breakdown of the device (Figure S8a), which possibly results from the unevenness and pinholes of the layers in the MIS devices (Figure S8b). As shown in Figure S9, I_{ohm} increased almost linearly with U_{app} at a relatively low applied voltage (U_{app}), indicating that the breakdown ohmic resistance was nearly constant and therefore renders the linear baseline fit feasible (Figure S13). However, when U_{app} was larger than the threshold voltage (∼3 V), the linearity between U_{app} and I_{ohm} collapsed, indicating a progressive breakdown. In this paper, we set the extraction voltage and its slope appropriately, ensuring that for most devices the extraction peak ends at when the instantaneous voltage is still small (<3 V, vide infra), and therefore I_{ohm} is precisely calibrated.

Figure 2a shows a schematic of the applied voltage profile and the induced I under the conventional CELIV framework (the typical CELIV result shown in Figure S10a), where a negative injection voltage (U_{inj}) for charge injection was immediately applied, generating a very large voltage slope ($d\,U_{inj}(t)/d\,t$, denoted as A'_{inj}) and therefore a large injection

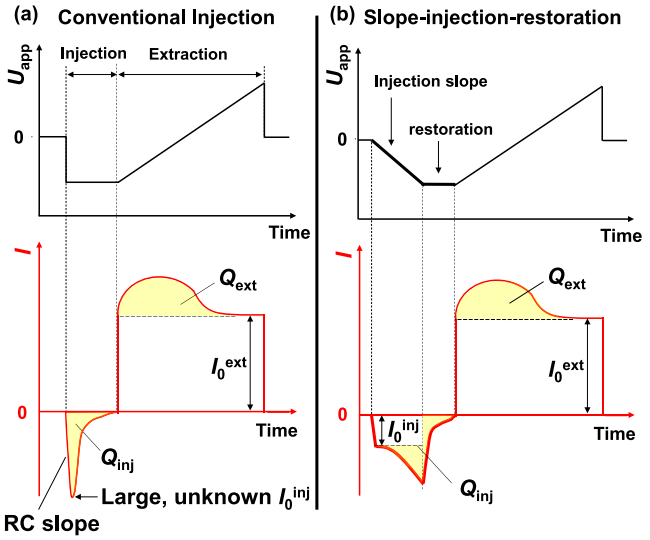

Figure 2. Schematic illustration of a conventional injection CELIV waveform (a) and a slope-injection-restoration CELIV waveform (b). The upper panel shows the applied voltage waveform, and the corresponding bottom panel shows the CELIV transient currents. The yellow region marks the amount of injected charge (Q_{inj}) or the amount of extracted charge (Q_{ext}). The injection current plateau (I_0^{inj}) and extraction current plateau (I_0^{ext}) are marked by arrows. The RC slope refers to the delay of the current response, indicating the RC constant.

https://doi.org/10.1021/acsomega.3c09977
ACS Omega 2024, 9, 26951−26962

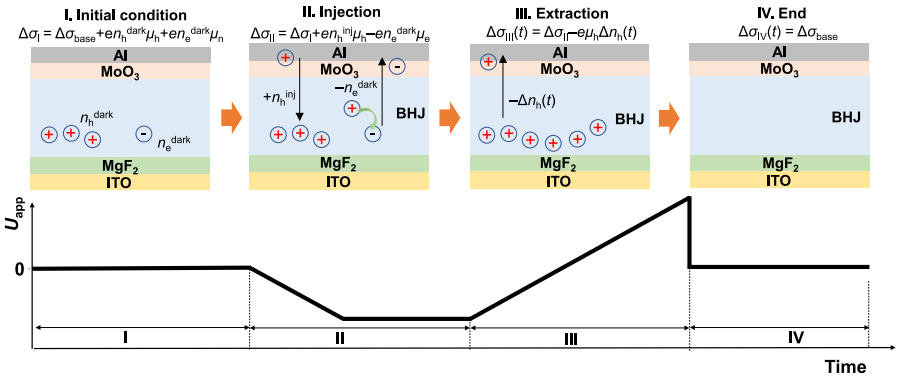

Figure 3. Schematic model of the charge carrier motion in an HOD during a CELIV measurement cycle (I–IV). The corresponding voltage periods are shown in the plot below. The $\Delta\sigma$ is shown at the top of each graph.

current plateau (I_0^{inj}; $I_0^{inj} \propto A'_{inj}$). However, this I_0^{inj} was hard to obtain or observe owing to the unknown A'_{inj} and RC delay of the current response. In the conventional calculation of Q_{inj}, I_0^{inj} is usually regarded as zero, which leads to overestimation of Q_{inj} (*i.e.* I_0^{inj} should be subtracted from the total current for an accurate Q_{inj} calculation). To overcome this issue, we adopted a linearly changing injection voltage as shown in Figure 2b, where a moderately designed A'_{inj} (in this paper, -2×10^4 V s^{-1}) renders a clear observation of the I_0^{inj} (the typical result shown in Figure S10b). Furthermore, considering the relatively short injection time (~100 μs), a so-called "restoration time" of 1 ms was applied following the injection slope, where the voltage was maintained at U_{inj} (voltage at the end of injection slope). The adoption of this 1 ms restoration time allows for full injection and thermalization[29] of the injected carriers, while imitating the trap-filling condition of real-operating OSCs (detailed discussion in the Supporting Note S2). Note that a variation of the restoration time between 0.2 and 2 ms has little effect on the CELIV and TRMC extraction signals (Figure S11), showing that a 1 ms restoration time can be universally applied for studying our OSC materials and comparing their time-dependent mobility characteristics. Moreover, it is often debatable whether such a "sufficiently relaxed" carrier mobility after ~1.1 ms injection time (injection slope + restoration time) is of any worth for dynamic characterization (since the typical mobility relaxation occurs within 10 μs after photogeneration).[18] For clarity, we illustrate the significance of the "late stage" mobility dynamics using Figure S12, addressing the difference in the charge injection mechanism of our MIS-CELIV measurement (electric-field injection) compared with that in real solar cells (photo injection). Before external bias is applied (Figure S12a), the trap density of states (trap DOSs) of semiconductors distributes near the conduction band of semiconductors. During electric-field injection (Figure S12b), the conduction band of semiconductor bends downward to the insulator and electrons are injected to the semiconductor/insulator interface, allowing for an unoccupied region of trap DOSs. These unoccupied trap DOSs still exist even after a long restoration time when the injected electrons are fully thermalized to the conduction band (Figure S12c). During extraction (Figure S12d), conduction band bends upward to the insulator as the cathode is positively biased, rendering the exposure of previously unoccupied trap DOSs and relaxation of carrier mobility through carrier hopping between them (similar to what happens shortly after photogeneration). Thus, studying the late-stage mobility dynamics during MIS-CELIV processes provides information about the trap states and their distribution, even with a long injection time.

An MIS device under an appropriate applied external voltage and the choice of charge transport layer can accumulate one type of charge carrier (hole or electron) in an ideal scenario. However, this is not the case with a real system, and $\Delta\sigma$ must be considered as the time-dependent, separate contributions from both electrons and holes as expressed using eq 3:[50]

$$\Delta\sigma(t) = en_e(t)\mu_e(t) + en_h(t)\mu_h(t) \tag{3}$$

where $n_e(t)$ and $n_h(t)$ are the temporal carrier densities of electrons and holes, respectively, and $\mu_e(t)$ and $\mu_h(t)$ are the temporal mobilities of electrons and holes, respectively. Moreover, a dark density of carriers generated by thermal activation and/or unintentional doping was introduced.[50] The presence of dark carriers was evident from the CELIV profiles in the HOD, even without applying an injection voltage (Figure S14a). The major dark carrier was a hole in the HOD and an electron in the EOD. As illustrated in Figure 3 (HOD), holes are injected into the BHJ layer, whereas very few dark electrons are subject to either recombination with the injected holes or leakage into the electrode when the bias is sufficiently large (stages I and II). While the minority dark carrier of electrons has a negligible effect on the hole density determination, it does contribute to the initial $\Delta\sigma$ before injection. This hole injection forms a hole-only environment, which leads to hole extraction under a sufficiently large extraction voltage within a long period (~100 μs, stage III). However, it is important to determine the baseline of $\Delta\sigma$ ($\Delta\sigma_{base}$) that appears in dark-carrier-sensitive TRMC measurements. As shown in stage IV, the situation of the remaining charge carrier density is different from the initial situation before injection (stage I), which causes the different $\Delta\sigma_{base}$. From the above discussion, a dynamic mobility formula is proposed as in eq 4:

$$\mu(t) = \frac{\Delta\sigma(t) - \Delta\sigma_{base}}{\frac{1}{Sd}\cdot\left[Q_{dark} + Q_{inj} - \int_{t_0}^{t}(I(t') - I_0 - I_{ohm}(t'))\mathrm{d}\,t'\right]} \tag{4}$$

where Q_{dark} is the charge of residual dark carriers, S is the device area (45 mm^2), d is the BHJ layer thickness, and other parameters have the same meaning as stated above. Q_{dark} was determined by directly applying an extraction bias, without injection, to fully extract the carriers (Figure S14a). Therefore, Q_{dark}, Q_{inj}, and Q_{ext} were experimentally determined by

https://doi.org/10.1021/acsomega.3c09977
ACS Omega 2024, 9, 26951−26962

Table 1. Comparison of the Q_{dark}, Q_{inj}, and Q_{ext} Measured Using Conventional and Slope-Restoration-Injection Strategies[a]

		conventional strategy[b]			slope-injection-restoration strategy[c]		
U_{inj} (V)	Q_{dark} [10^{-8} C]	Q_{inj} [10^{-8} C]	Q_{ext} [10^{-8} C]	$Q_{ext}/(Q_{dark} + Q_{inj})$	Q_{inj} [10^{-8} C]	Q_{ext} [10^{-8} C]	$Q_{ext}/(Q_{dark}+Q_{inj})$
−2	0.0428	4.54	2.58	0.56	3.08	2.96	0.95
−4	0.0428	13.1	8.14	0.62	7.60	8.48	1.11
−6	0.0428	17.7	15.0	0.84	13.1	15.6	1.18
−8	0.0428	24.9	24.8	1.00	19.9	26.4	1.33
−10	0.0428	33.3	30.8	0.92	28.7	41.4	1.44

[a]The device is a PM6:Y6 HOD device. [b]$A'_{ext} = 10^5$ V s^{-1}, voltage at the end of the extraction slope (U_{ext}) = 10 V. [c]$A'_{inj} = -2 \times 10^4$ V s^{-1}, $A'_{ext} = 10^5$ V s^{-1}, restoration time = 1 ms, and U_{ext} = 10 V.

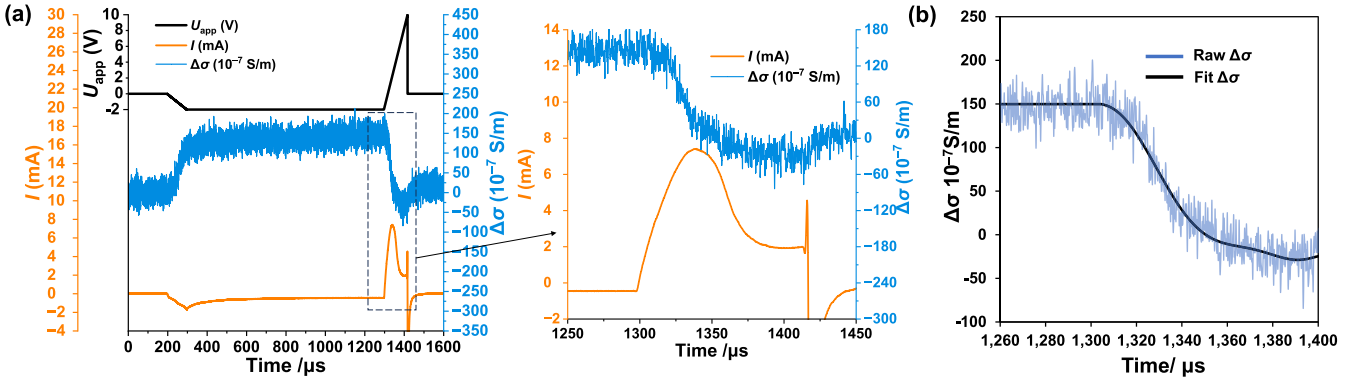

Figure 4. (a) Left: CELIV-TRMC results of a typical slope-injection-restoration measurement in a P3HT:PCBM HOD with a raw TRMC signal ($\Delta\sigma$, blue line) and a CELIV transient current (I, orange line). The black line shows the applied voltage ($A'_{inj} = -2 \times 10^4$ V s^{-1}, $U_{inj} = -2$ V, restoration time = 1 ms, $A'_{ext} = 10^5$ V s^{-1}, and U_{ext} = 10 V). Right: enlarged picture of the dashed box area showing the stage of charge extraction. (b) Comparison of the 8-order polynomial function fit curve (black line) and the raw $\Delta\sigma$ signal in (a), where only the extraction part is shown for ease of demonstration.

analyzing the CELIV current. In the case of devices with non-negligible I_{ohm}, the current baseline was fitted as shown in Figure S13b. As previously mentioned in this section, t_0 is solely an estimate of the beginning of charge extraction, and the error in estimated $\mu(t)$ is within 10% (see Supporting Information Section 1 for detail). Moreover, to avoid overestimation of the mobility (especially when $Q_{inj} + Q_{dark} \approx Q_{ext}$), the late stage of extraction (i.e., >3/4 of the total extraction time, ∼30−40 μs varied by samples) is usually neglected for better accuracy. This is because in such a late stage the both the remaining charge (denominator term in eq 4) and the $\Delta\sigma - \Delta\sigma_{base}$ can reach 0, while the fluctuation of $\Delta\sigma - \Delta\sigma_{base}$ due to a small S/N ratio can cause the mobility to unreasonably shift to infinitive.

Table 1 lists a comparison of the measured Q_{dark}, Q_{inj}, and Q_{ext} values in the PM6:Y6 HOD using conventional constant injection and slope-restoration-injection voltages. At relatively small injection voltages ($|U_{inj}| \leq 6$ V), the Q_{ext} $(Q_{dark} + Q_{inj})^{-1}$ is almost unity in the slope-injection-restoration strategy, whereas the constant-voltage injection shows a clear deviation from unity, indicating overestimation of Q_{inj}. At a high injection voltage ($(|U_{inj}| > 6$ V), Q_{ext} $(Q_{dark} + Q_{inj})^{-1}$ is considerably increased despite the type of voltage profile owing to the increased device breakdown and large I_{ohm}. Therefore, in the CELIV-TRMC measurement, a small injection voltage with a slope-restoration-injection profile is preferable to accurately determine the carrier density and prevent breakdown. The interpolated slope of Q_{inj} vs U_{inj} (−2 to −10 V) in the slope-restoration-injection voltage profile was $|Q_{inj}/U_{inj}| = 2.55 \times 10^{-8}$ C V^{-1}, which was consistent with the capacitance of the device (2.19×10^{-8} C V^{-1}) based on the insulator thickness (100 nm), the typical relative permittivity (5.5), and the device area and supported the validity of the measurements.

To verify the reliability of our CELIV-TRMC mobility, the conventional MIS-CELIV average mobility (μ_{CELIV}) was also calculated using eq 5:[52]

$$\mu_{MIS-CELIV} = \frac{2d_s^2}{A' t_{max}^2}\left(1 + \frac{\varepsilon_s d_i}{\varepsilon_i d_s}\right) \quad (5)$$

where A' is the slope (ramp) of the extraction voltage, t_{max} is the time difference between the extraction current peak and the beginning point of charge extraction, d_s and d_i refer to the thicknesses of semiconductor layer and insulator layer, respectively. ε_s and ε_i refer to the relative permittivity of the semiconductor and insulator layers, respectively. In this paper, the MgF_2 insulator layer for all HODs was 50 nm, and the LiF insulator layer for all EODs was 100 nm. The relative permittivity is 7.6 for MgF_2,[55] 8.3 for LiF,[56] 3.5 for P3HT:PCBM,[57] 4.95 for PffBT4T:PCBM,[58] 3.71 for PM6:ITIC,[59] 3.99 for PM6:IT4F,[59] and 3.94 for PM6:Y6.[59]

2.3. CELIV-TRMC Results of HODs. Figure 4a shows typical CELIV-TRMC transients of a P3HT:PCBM HOD using magnesium fluoride (MgF_2) as the insulator and molybdenum oxide (MoO_3) as the hole transport layer. At t = 190 μs, a negative injection slope was applied to inject holes into the BHJ layer, giving rise to I and $\Delta\sigma$. At t = 290 μs, the injection voltage slope switched to steady voltage and the displacement current plateau (I_0) gradually disappeared while charge injection continued. The charge injection then saturated at $t \sim 500$ μs as I gradually stabilized to I_{ohm}, and

https://doi.org/10.1021/acsomega.3c09977
ACS Omega 2024, 9, 26951−26962

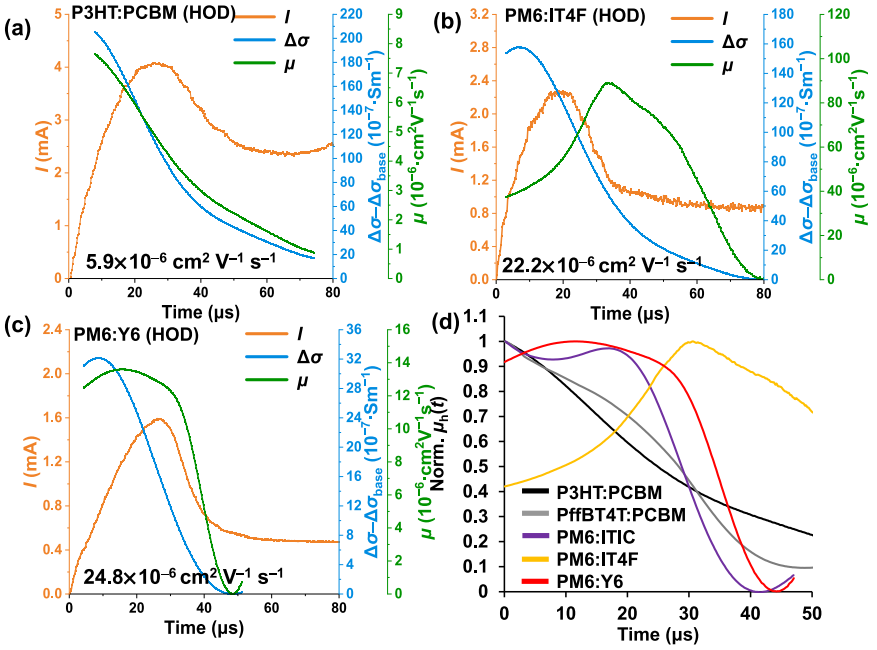

Figure 5. Plots of the measured CELIV-TRMC transients of HODs and the time-dependent μ_h: (a) P3HT:PCBM, (b) PM6:IT4F, and (c) PM6:Y6. The TRMC signals are shown as $\Delta\sigma - \Delta\sigma_{base}$, where the $\Delta\sigma_{base}$ values are listed in Table S2. The μ_{CELIV} values of each sample is appended. The voltage conditions were $A'_{inj} = -2 \times 10^4$ V s^{-1}, $U_{inj} = -2$ V, restoration time = 1 ms, $A'_{ext} = 10^5$ V s^{-1}, and $U_{ext} = 10$ V. For ease of expression, the time was set to zero at the start of the extraction slope. (d) Summary of the normalized μ_h for all the five BHJs as a function of extraction time.

Table 2. Summary of $\mu_{1/2}$, $\tau_{1/2}$, and μ_{CELIV}, and the BHJ Thickness of the HODs Measured Using the Slope-Injection-Restoration Strategy[a]

sample (HOD)	$\mu_{1/2}$[b] [10^{-6} cm^2 V^{-1} s^{-1}]	$\tau_{1/2}$[c] [μs]	μ_{CELIV} [10^{-6} cm^2 V^{-1} s^{-1}]	d_{BHJ}[d] [nm]
P3HT:PCBM	3.84	24.8	5.91	139 ± 16
PffBT4T:PCBM	23.1	28.2	14.6	148 ± 27
PM6:ITIC	10.9	28.8	16.8	185 ± 18
PM6:IT4F	19.1	65.4	22.2	144 ± 28
PM6:Y6	6.20	34.8	24.9	279 ± 32

[a]All HOD devices were measured at $U_{inj} = -2$ V, $A'_{inj} = -2 \times 10^4$ V s^{-1}, $A'_{ext} = 10^5$ V s^{-1}, restoration time = 1 ms, and $U_{ext} = 10$ V. [b]Half of the initial CELIV-TRMC mobility. [c]Time at half of the initial CELIV-TRMC mobility. [d]Averaged over at least 10 measurements using a surface profiler.

at the same time the marginal increase of $\Delta\sigma$ also appeared to cease. At $t \sim 1290$ μs, the extraction slope started and a typical extraction current peak was observed, whereas $\Delta\sigma$ decreased due to the decrease in hole density and/or mobility. Interestingly, $\Delta\sigma$ decreased to a considerably lower value than the initial baseline before injection, indicating the extraction of residual dark carriers. Finally, the carriers were almost fully extracted, and $\Delta\sigma$ stopped decreasing. The responses of $\Delta\sigma$ and I under the applied bias matched well with those of our model shown in Figure 3, supporting the feasibility of our mobility determination. However, the signal-to-noise ratio of the TRMC signal was low because of the relatively small A of the transmission TRMC cavity, in addition to the intrinsically low carrier mobility, which was different from that of nonrelaxed charge carriers generated by pulsed light. To reduce the high-frequency fluctuation of $\Delta\sigma$, a fitting with an 8-order polynomial function was applied (Figure 4b). This allows for the suppression of noise amplification when $\Delta\sigma$ is divided by the reduced charge density on the delayed time scale of charge extraction. The fitting results for the other HODs and EODs are provided in Figures S15 and S16.

The CELIV-TRMC transients of the HODs (P3HT:PCBM, PM6:IT4F, and PM6:Y6) during the charge extraction process of the slope-injection-restoration method (U_{inj} of -2 V) are shown in Figure 5a–c, respectively (the data of the other devices, namely, PffBT4T:PCBM and PM6:ITIC, are shown in Figure S17). The start time of charge extraction was shifted to zero for clarity, and the TRMC signal is shown as $\Delta\sigma - \Delta\sigma_{base}$. Here, we observed that in most devices measured in this work, the rising part of CELIV extraction current before the peak did not follow a superlinear shape as can be typically seen in other MIS-CELIV measurements. The observed more gradual rising shape of extraction current can be attributed to two reasons: i. the nonideal surface distribution of injected charge carriers (schematized in Figure S18), whose effect becomes more significant in our thin-film devices (BHJ thickness of 100–300 nm); ii. the existence of dark equilibrium carriers that follow a homogeneous distribution (Figure S19a). The time-dependent TRMC mobility was calculated using eq 4. It is noteworthy that the obtained time-dependent mobilities are mostly in the order of 10^{-6}–10^{-5} cm^2 V^{-1} s^{-1}, which corresponds with the delayed photo-CELIV mobilities[40] and originates from the

https://doi.org/10.1021/acsomega.3c09977
ACS Omega 2024, 9, 26951–26962

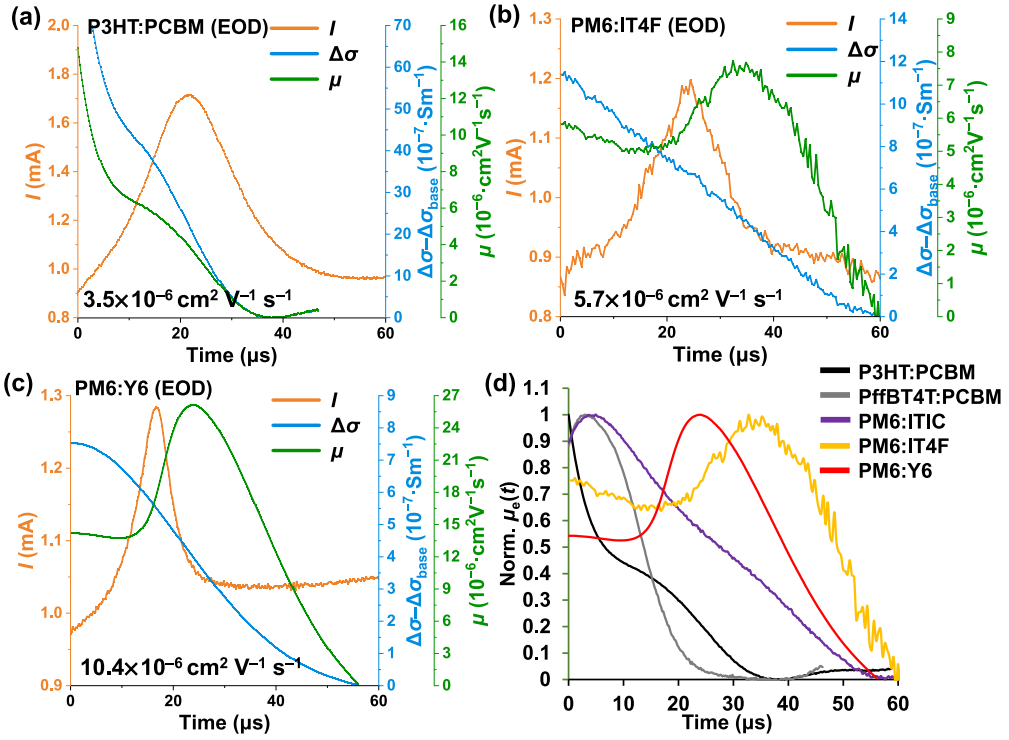

Figure 6. Plots of the measured CELIV-TRMC transients of EODs and the time-dependent μ_e: (a) P3HT:PCBM, (b) PM6:IT4F, and (c) PM6:Y6. The TRMC signals are shown as $\Delta\sigma - \Delta\sigma_{base}$, where the $\Delta\sigma_{base}$ values are listed in Table S4. The μ_{CELIV} of each sample is appended. Here, $U_{inj} = -2$ V for (a,c) and $U_{inj} = -6$ V for (b), and other voltage conditions are the same: $A'_{inj} = -2 \times 10^4$ V s^{-1}, restoration time = 1 ms, $A'_{ext} = 10^5$ V s^{-1}, and $U_{ext} = 10$ V. For ease of expression, the time was set to zero at the start of the extraction slope. (d) Summary of the normalized μ_e for all five BHJs as a function of extraction time.

long injection time (1.1−1.2 ms) as previously discussed. The obtained Q_{ext} $(Q_{dark} + Q_{inj})^{-1}$, hole μ_{CELIV}, half-life of TRMC mobility decay ($\tau_{1/2}$), half value of TRMC mobility ($\mu_{1/2}$), and thicknesses of the devices are listed in Table 2 (Q_{dark}, Q_{inj}, Q_{ext}, and $\Delta\sigma_{base}$ are listed in Table S1). All samples exhibited typical CELIV extraction peaks with a clear plateau of I_0^{ext}, indicating that the charge extraction was sufficient. As shown in Figure 5d, the polymer:fullerene BHJs (P3HT:PCBM and PffBT4T:PCBM) exhibited a prompt decrease in μ_h, whereas the high-performing NFA BHJs exhibited a significantly slower μ_h decay. During the first 30 μs of extraction, the μ_h values of both P3HT:PCBM and PffBT4T:PCBM decreased by approximately 2.5-fold (from 7.6×10^{-6} to 3.1×10^{-6} cm^2 V^{-1} s^{-1} for P3HT:PCBM and from 44.4×10^{-6} to 18.0×10^{-6} cm^2 V^{-1} s^{-1} for PffBT4T:PCBM), which corresponds with the comparatively small hole μ_{CELIV} (5.9×10^{-6} and 14.6×10^{-6} cm^2 V^{-1} s^{-1} for P3HT:PCBM and PffBT4T:PCBM, respectively). The decrease in mobility can be attributed to mainly three reasons (more details in Supporting Note S3): (i) mobility relaxation due to charge transport via carrier hopping into deeper trap states, as revealed by Melianas et al;[18] (ii) sequential charge extraction, where the faster carriers with higher mobility are extracted prior to the slower carriers; (iii) mobility difference between injected carriers (uneven distribution, Figure S19a) and dark equilibrium carriers (even distribution), where the latter shows ∼4 times larger initial mobility compared to the former (Figure S19b). The lower μ_h of P3HT:PCBM than that of PffBT4T:PCBM also match with our previous TOF mobility results (1.8×10^{-3} cm^2 V^{-1} s^{-1} for P3HT:PCBM and 1.4×10^{-2} cm^2 V^{-1} s^{-1} for PffBT4T:PCBM),[31,33] whereas the order difference was mainly due to the difference in the measurement time scale[18] and carrier injection method.[60] For the NFA BHJ samples, PM6:ITIC exhibited a very stable μ_h of ∼22.2×10^{-6} cm^2 V^{-1} s^{-1} during the first 30 μs, which is close to its μ_{CELIV} (16.8×10^{-6} cm^2 V^{-1} s^{-1}), indicating that the hole mobility in PM6:ITIC is very stable throughout the transport process. PM6:Y6 exhibited a stable μ_h during the first 40 μs, while the initial μ_h (∼13.3×10^{-6} cm^2 V^{-1} s^{-1}) was lower compared with μ_{CELIV} (24.8×10^{-6} cm^2 V^{-1} s^{-1}). Such deviations can be attributed to the nonideal surface distribution of the injected carriers due to carrier diffusion,[61] resulting in underestimation of the t_{max} and therefore overestimation of μ_{CELIV}. Still, the μ_{CELIV} values provide important references to validate our CELIV-TRMC mobilities. Interestingly, the PM6:IT4F exhibited an increase in μ_h during the first 35 μs, which likely resulted from the vertical gradient of the polymer/NFA BHJ and charge detrapping through the Poole−Frenkel framework, which facilitates an efficient transport route.[62−66] Comprehensively, the CELIV-TRMC mobility dynamics during charge extraction is the result of trade-offs between the positive factors (such as Poole−Frenkel effect and the vertical composition gradient) and the negative factors (such as hopping in the trap states, the extraction sequence, and dark carriers). Q_{dark} in P3HT:PCBM HOD (3.03×10^{-8} C) was significantly larger than that in other better-performing BHJs (<0.2×10^{-8} C), which indicates a significantly higher density of defect-related trap states in P3HT:PCBM.

The CELIV-TRMC results of the slope-injection strategy without restoration are shown in Figure S20 and Table S2, whose μ_h characteristics show a similar trend as compared to that of the slope-injection-restoration strategy. The μ_h value

https://doi.org/10.1021/acsomega.3c09977
ACS Omega 2024, 9, 26951−26962

Table 3. Summary of $\mu_{1/2}$, $\tau_{1/2}$, μ_{CELIV}, and the BHJ Thickness of the EODs Measured Using the Slope-Injection-Restoration Strategy

sample (EOD)	$\mu_{1/2}$ [10^{-6} cm^2 V^{-1} s^{-1}]	$\tau_{1/2}$ [μs]	μ_{CELIV} [10^{-6} cm^2 V^{-1} s^{-1}]	d_{BHJ}[c] [nm]
P3HT:PCBM[a]	7.18	7.0	3.51	113 ± 27
PffBT4T:PCBM[a]	11.3	14.6	5.88	80 ± 10
PM6:ITIC[b]	0.884	31.4	1.42	96 ± 16
PM6:IT4F[b]	3.00	51.6	5.71	99 ± 14
PM6:Y6[a]	7.11	45.2	10.4	157 ± 21

[a]All EOD devices were measured at U_{inj} = −2 V, A'_{inj} = −2 × 10^4 V s^{-1}, A'_{ext} = 10^5 V s^{-1}, restoration time = 1 ms, and U_{ext} = 10 V. [b]All EOD devices were measured at U_{inj} = −6 V, A'_{inj} = −2 × 10^4 V s^{-1}, A'_{ext} = 10^5 V s^{-1}, restoration time = 1 ms, and U_{ext} = 10 V. [c]Averaged over at least 10 measurements using a surface profiler.

was slightly larger for the slope-injection strategy, which may arise from the relatively short injection time, allowing for a certain proportion of unthermalized injected charge carriers. The calculated charges of the slope-injection strategy in the PM6:Y6 HOD under various $|U_{inj}|$ values are listed in Table S3. The $Q_{ext}/(Q_{dark} + Q_{inj})$ values under a low $|U_{inj}|$ were very close to unity, showing good accuracy for charge density determination, similar to those achieved by the slope-injection-restoration strategy. However, Q_{inj} was smaller at a low $|U_{inj}|$ for the slope-injection strategy, which is disadvantageous for minimizing the effect of residual dark electrons. Therefore, the slope-injection-restoration strategy is more suitable for our CELIV-TRMC measurements.

2.4. CELIV-TRMC Results of EODs. Compared with the HOD structure, finding an appropriate EOD structure for reliable CELIV-TRMC measurements is more complicated. After examining the device structure (top or bottom insulator), insulator (thick MgF_2 or lithium fluoride (LiF)), and electron transport layer (LiF, ZnO, bathocuproine (BCP), or 3,3′-(1,3,8,10-tetraoxoanthra[2,1,9-*def*:6,5,10-*d′e′f′*]diisoquinoline-2,9(1H,3H,8H,10H)-diyl)bis(*N*,*N*-dimethylpropan-1-amine oxide):PDINO), it was found that the EOD with a 10 nm PDINO electron transport layer yielded a reasonable CELIV-TRMC result, which resembles the signals in our HOD measurements (the details of the examination are provided in Figures S21−S24). The CELIV-TRMC results of the EODs (P3HT:PCBM, PM6:IT4F, and PM6:Y6) during the charge extraction process of the slope-injection restoration method are shown in Figure 6a−c, respectively, whereas the data for the other devices, that is, PffBT4T:PCBM and PM6:ITIC, are provided in Figure S25 (Q_{dark}, Q_{inj}, Q_{ext}, and $\Delta\sigma_{base}$ are listed in Table S4). The PM6:ITIC and PM6:IT4F EODs were injected under a relatively large U_{inj} of −6 V because of the very small Q_{inj} at U_{inj} = −2 V. For the other EODs, U_{inj} = −2 V was sufficient for the CELIV-TRMC measurements. It is noteworthy that compared with HODs, the extraction current curves of EODs show a relatively more superlinear rise shape (especially in well-performing PM6:IT4F and PM6:Y6), which may indicate a more significant surface distribution of injected carriers and therefore larger error in the CELIV-TRMC mobility. However, according to G. Juška et al.,[67] such a difference in the rise shape of extraction currents possibly originates from the more electric field dependence of mobility in EODs due to the Poole−Frenkel effect. This is possibly due to the BHJ layer being thinner than that of HODs by a factor of 0.3−0.5, the low electron trap density (consistent with the observed low Q_{dark}) and high crystallinity in nonfullerene-based OSCs, which mitigate the disorder-related decrease of mobility during extraction. Compared with HODs, the typically one-order lower injected charge (10^{-9} C) in EODs indicates a smaller effective injection field, which is considered to result from a difference in the energy alignment (such as larger injection barriers between the ETL and BHJ) and the BHJ nature. The smaller effective injection field in EODs leads to a more homogeneous and bulky charge carrier distribution, rendering possibly a smaller deviation between t_0 and the start point of carriers leaving the device and therefore more precise results of estimated charge and time-dependent mobility.

As shown in Figure 6d, the NFA BHJs showed more stable μ_e decays than those of polymer:fullerene with significantly larger $\tau_{1/2}$ values (>30 μs), as compared to the 7.0 μs for P3HT:PCBM and the 14.6 μs for PffBT4T:PCBM (Table 3). During the first 30 μs of extraction, the μ_e values of P3HT:PCBM and PffBT4T:PCBM decreased by more than 5-fold, which corresponds to their relatively smaller μ_{CELIV} values (∼1/4 and ∼1/5 of the initial μ_e for P3HT:PCBM and PffBT4T:PCBM, respectively). PM6:ITIC showed a slowly decreasing μ_e, with also a low μ_{CELIV} of 1.42 × 10^{-6} cm^2 V^{-1} s^{-1} (∼3/5 of the initial μ_e). Interestingly, PM6:Y6 and PM6:IT4F exhibited stable and even increasing μ_e characteristics with a relatively large μ_{CELIV} (10.4 × 10^{-6} cm^2 V^{-1} s^{-1} and 5.7 × 10^{-6} cm^2 V^{-1} s^{-1} for PM6:Y6 and PM6:IT4F, respectively), mainly due to the Poole−Frenkel effect. Additionally, both the μ_{CELIV} of PM6:Y6 and PM6:IT4F matched well with its initial μ_e (∼13.9 × 10^{-6} cm^2 V^{-1} s^{-1} and 5.8 × 10^{-6} cm^2 V^{-1} s^{-1} for PM6:Y6 and PM6:IT4F), evidencing on their stable and even increasing μ_e during electron transport.

2.5. Dynamic Hole/Electron Mobility Ratios Revealed by CELIV-TRMC Measurements. Finally, the dynamic mobility balance (μ_e/μ_h) of the five BHJs (Figure 7) was

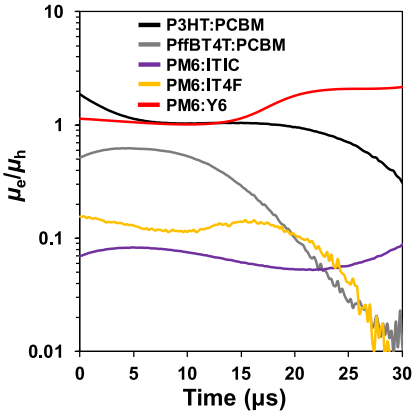

Figure 7. Plot of dynamic μ_e/μ_h obtained from Figures 5d and 6d. Time starts at the beginning of charge extraction. For ease of illustration, only the first 30 μs range is shown.

https://doi.org/10.1021/acsomega.3c09977
ACS Omega 2024, 9, 26951−26962

calculated using the data shown in Figures 5d and 6d. This study is the first to report purely experimental time-dependent electron/hole mobility ratios in thin-film BHJ OSCs within tens of microseconds (typical charge extraction time). Within the first 20 μs, PM6:ITIC exhibited a very unbalanced μ_e/μ_h of ~0.07, while PM6:IT4F exhibited a slightly more balanced μ_e/μ_h of ~0.15. The other BHJs exhibited a moderately balanced μ_e/μ_h of 0.5−2.0. Given their OSC performances (Table S5; the current density−voltage curves and external quantum efficiency spectra are provided in Figure S26), the following conclusions can be reached. (i) The lower FF of P3HT:PCBM (maximum value = 0.616), as compared with PffBT4T:PCBM (maximum value = 0.663), was mainly attributed to the lower μ_e and μ_h values of P3HT:PCBM (differed by a factor of approximately 2−5, as compared to PffBT4T:PCBM), whereas both exhibited a balanced charge transport due to the μ_e/μ_h of approximately 0.5−2.0. Additionally, the large carrier trap density in P3HT:PCBM revealed by the large Q_{dark} in the HOD (~3.03×10^{-8} C) suggests a higher degree of charge recombination within the BHJ, which leads to a lower FF. (ii) The very unbalanced μ_e/μ_h (<0.1) and very small μ_e value in PM6:ITIC resulted in an unsatisfactory FF (0.612), whereas the FF of PM6:IT4F (~0.691) outweighed that of PM6:ITIC due to a slightly improved mobility balance ($\mu_e/\mu_h \sim 0.15$) and larger dynamic μ_e and μ_h (differed by a factor of approximately 2−4, as compared to PM6:ITIC). (iii) The highest FF in PM6:Y6 (0.734) was attributed to both a balanced dynamic mobility ratio ($\mu_e/\mu_h \sim 1.0-1.1$) and relatively large mobility values (both μ_e and $\mu_h \sim 14 \times 10^{-6}$ cm^2 V^{-1} s^{-1}), which may also explain its extraordinary long electron-diffusion length (~330 nm).[68] It is noteworthy that due to the fixed OSC device structure (ITO/ZnO/BHJ/MoO_3/Ag), the FF factor of each OSC was not necessarily its optimal value owing to the material-specific energy level alignment. However, this has no impact on studying the FF versus $\mu(t)$ correlation, as the MIS-CELIV device structures were properly chosen to resemble the charge carrier transport in the OSCs. Overall, the unique CELIV-TRMC technique with an MIS device that enables the simultaneous evaluation of the dynamic TRMC μ_e, μ_h, and their balance as well as CELIV mobility (μ_{CELIV}) can provide an in-depth understanding of the transport process of electric-field-injected charge carriers in thin film OSCs, which is correlated to their FF values.

3. CONCLUSIONS

This study demonstrated a new CELIV-TRMC technique for the determination of time-dependent charge carrier mobility in thin-film OSCs. The advantages of this measurement include its purely experimental basis, suitability for thin-film active layers, and the implementation of separate measurements for electrons and holes. Along with a precise determination of sensitivity factor ($A \sim 13$ m S^{-1}) of a transmission-type cavity with a MIS device, the authors proposed a slope-injection-restoration profile to improve the accuracy of the injected charge evaluation and the formula for the CELIV-TRMC mobility. The dynamic μ_e and μ_h values of the five BHJs were determined by using CELIV-TRMC. The accuracy of calculated CELIV-TRMC mobilities was validated by their good matches with the MIS-CELIV time-averaged mobilities. For conventional polymer:fullerene BHJs, P3HT:PCBM and PffBT4T:PCBM exhibited both a fast-decaying μ_h (~2.5-fold) and μ_e (>5-fold) within the first 30 μs of charge extraction. A good contrast was found for the well-performing NFA OSCs (PM6:ITIC, PM6:IT4F, and PM6:Y6) with significantly more stable μ_h and μ_e characteristics within the 30 μs range. In particular, the high-performing PM6:Y6 exhibited a balanced dynamic μ_e/μ_h (~1.0−1.1), relatively large mobility values (~6×10^{-6} cm^2 V^{-1} s^{-1} for both μ_e and μ_h), and good correspondence with the high FF, large optimal thickness range, and long diffusion length. Additionally, the CELIV and TRMC mobilities exhibited good consistency, confirming the feasibility of the CELIV-TRMC measurements. This newly developed technique may also apply to more complicated solar cell systems, such as ternary OSCs, additive-variable OSCs, and surface-passivated perovskite solar cells, assisting in the performance study and device optimization.

4. EXPERIMENTAL SECTION

4.1. Materials. Regioregular P3HT was purchased from Sigma-Aldrich. PffBT4T (also known as PffBT4T-2OD), IT4F (also known as ITIC-4F), ITIC, Y6, and PM6 (also known as PBDBT-2F) were purchased from 1-Material Inc. $PC_{61}BM$ (PCBM; purity >99.5%) was purchased from Frontier Carbon Inc. CB (purity >99.5%) was purchased from Kishida Chemical Co. Ltd. CF (superhydrated, purity >99.0%), methanol (MeOH; superhydrated, purity >99.8%), and *o*-dichlorobenzene (DCB; purity >98.0%) were purchased from Fujifilm Wako Pure Chemical Corp. All the solvents were used as received without further purification. 1,8-Diiodooctane (DIO; purity >98%) was purchased from Sigma-Aldrich. BCP (purity >99.0%) and 1-chloronaphthalene (CN; purity >97%) were purchased from Tokyo Chemical Industry Co., Ltd. PDINO was purchased from Ossila Co. Ltd. LiF (purity >99.9%), MgF_2 (purity 99.9%), and MoO_3 (purity 99.98%) were purchased from Japan Pure Chemical Co. Ltd. A quartz/ITO substrate was purchased from GEOMATEC Co., Ltd.

4.2. BHJ Layer Preparation. Five BHJ layers were prepared according to the optimal preparation conditions reported in the literature.[4,33,69,70] The BHJ solution preparation and layer deposition were conducted inside an N_2-filled glovebox. For the BHJ layer deposition, ~ 70 μL of the BHJ solution was cast onto each sample and rotated at a certain speed, followed by annealing on a hot plate (see below). For P3HT:PCBM = 1:1 (in a weight ratio), a DCB solution of 2.2 wt % was prepared and stirred at 70 °C for 5 h, followed by spin coating at 1500 rpm for 15 s and drying at 150 °C for 10 min. For PffBT4T:PCBM = 1:1.2 (with 3 vol % DIO), a DCB solution of 1.4 wt % was prepared and stirred at 110 °C for 7 h, followed by spin coating at 1000 rpm for 15 s and drying at 100 °C for 10 min. For PM6:ITIC = 1:1 or PM6:IT4F = 1:1, CB solutions of 1.1 wt % with 0.5 vol % DIO were prepared and stirred at 70 °C for 7 h, followed by spin coating at 1700 rpm for 15 s and then drying at 100 °C for 10 min. For PM6:Y6 = 1:1.2, a CF solution of 1.1 wt % with 0.5 vol % CN was prepared and stirred at 70 °C for 7 h, followed by spin coating at 3000 rpm for 30 s and drying at 110 °C for 10 min.

4.3. MIS Device Fabrication. A bottom-insulator MIS structure was adopted for the HOD. A top-insulator MIS structure was adopted for the EOD. First, an ITO-patterned quartz substrate (60 mm × 8 mm × 1 mm patterned using 150 nm-thick ITO; ~15 Ω sq^{-1}) was subjected to sequential ultrasonic treatments in detergent, acetone, and isopropanol for 15 min each, followed by UV-ozone cleaning for 10 min. Subsequently, a 100 nm-thick Al guide electrode was deposited onto the substrate with a shadow mask in a vacuum chamber (thermal evaporation; 3−5 Å s^{-1}). For an HOD, a 50 nm-thick

https://doi.org/10.1021/acsomega.3c09977
ACS Omega 2024, 9, 26951−26962

MgF_2 insulator was deposited (thermal evaporation; 0.5−1 Å s^{-1}) followed by the deposition of the BHJ layer, a 10 nm-thick MoO_3 hole transport layer (thermal evaporation; 0.1−0.2 Å s^{-1}), and a 60 nm-thick Al top electrode (thermal evaporation; ∼2 Å s^{-1}). For an EOD, an ∼10 nm-thick PDINO electron transport layer was deposited by casting 100 μL of PDINO solution (1 mg mL^{-1} in super dehydrated MeOH) and rotating at 3000 rpm for 30 s, followed by drying at room temperature for 5 min and subsequent BHJ layer deposition. Subsequently, a 100 nm-thick LiF insulator was deposited (thermal evaporation; 0.5−1 Å s^{-1}) followed by deposition of a 60 nm-thick Al top electrode (thermal evaporation; ∼2 Å s^{-1}).

4.4. CELIV-TRMC Measurement. A harmonic transmission-type resonant cavity (TE_{10m}, m = 14) was used, which was the same as that used in a previous report.[34] The TRMC signals were probed using continuous microwaves (∼9.16 GHz, ∼50 mW) generated using a microwave signal generator (SMB100A, Rohde and Schwarz, Munich, Germany). Such a low microwave power is considered to have a negligible effect on the charge-carrier motion. For the CELIV measurements, a waveform generator (Keysight 33 500 B) was used to apply the designed voltage signal to the device. In a typical slope-injection CELIV measurement, a linearly increasing negative voltage (the voltage at the end of the injection slope was varied from 0 to −10 V) was first applied to the device at a small ramp (A' = 2 × 10^4 V s^{-1}), followed by a positive linearly increasing voltage to fully extract the carriers (the voltage at the end of the extraction slope was set at 10 V; A' = 1 × 10^5 V s^{-1}). For the restoration slope-injection CELIV measurement, a constant negative voltage, identical to the end voltage of the injection slope, was applied after the injection voltage (last time: 1 ms). Accordingly, the measurement time window was ∼1 ms, while a typical repetition rate of measurement was 10 Hz (100 ms interval) so as to maintain the initial charge balance (dark carrier). No baseline drift during averaging (512 traces) was observed. For both the bottom-insulator-type HOD and the top-insulator-type EOD, the bottom ITO with an Al guide electrode was connected to a waveform generator and the top Al electrode was connected to an oscilloscope (earth). The transient photocurrent signals between the bottom and top electrodes and the TRMC signals from a microwave detector were simultaneously recorded by using an oscilloscope (50 Ω termination; DPO4000, Tektronix, Oregon, United States). The effective contact area was 45 mm^2, as defined by the top Al electrode. All of the measurements were performed at 27 °C in air.

4.5. Organic Photovoltaic Device. A ZnO layer was fabricated onto a cleaned and ozone treated ITO layer by spin coating with a ZnO precursor solution (0.1 g/mL zinc acetate dihydrate and 0.028 g/mL ethanolamine in 2-methoxyethanol) at 4000 rpm/15 s. The precursor solution was heated to 60 °C for 1h and 3−4 h at room temperature at high rpm. The substrate was annealed on a hot plate at 200 °C for 30 min. An active layer was cast on top of the ZnO layer in a nitrogen glovebox by spin coating. An anode consisting of 15 nm MoO_x and 100 nm Ag layers was sequentially deposited on top of the active layers through a shadow mask by thermal evaporation in a vacuum chamber. The resulting device configuration was an ITO (120−160 nm)/ZnO (30 nm)/active layer (∼100 nm)/MoO_x (10 nm)/Ag (100 nm) with an active area of 7.1 mm^2. Current density−voltage curves were measured using a source-measure unit (ADCMT Corp., 6241A) under AM 1.5 G solar illumination at 100 mW cm^{-2} (1 sun, monitored by a calibrated standard cell, Bunko Keiki BS-520BK) from a 300 W solar simulator (SAN-EI Corp., XES-301S). The EQE spectra were measured using a Bunko Keiki model SM-250 KD instrument equipped with a Keithley model 2401 source meter. The monochromated light power was calibrated using a silicon photovoltaic cell, Bunko Keiki model S1337−1010BQ.

■ ASSOCIATED CONTENT

Supporting Information

The Supporting Information is available free of charge at https://pubs.acs.org/doi/10.1021/acsomega.3c09977.

The extraction start point, Q_{ext} and Q_{inj}, restoration time, and mobility relaxation (Supporting Notes S1−S3); Q_{ext}, Q_{inj}, Q_{dark}, and other experimental values (Tables S1−S4) and PCE and other parameters of OSC devices (Table S5); results and explanations of the CELIV-TRMC measurements, sensitivity factor determination (Figures S1−S3); schematics of CELV-TRMC, additional experimental details, and raw data (Figures S4−S20); CELIV-TRMC transients of other device structures (Figures S21−S25); J−V curves and EQE spectra of OSCs (Figure S26) (PDF)

■ AUTHOR INFORMATION

Corresponding Author

Akinori Saeki − *Department of Applied Chemistry, Graduate School of Engineering, Osaka University, Suita, Osaka 565-0871, Japan; Innovative Catalysis Science Division (ICS), Institute for Open and Transdisciplinary Research Initiatives (OTRI), Osaka University, Suita, Osaka 565-0871, Japan;* orcid.org/0000-0001-7429-2200; Phone: +81-6-6879-4587; Email: saeki@chem.eng.osaka-u.ac.jp

Authors

Shaoxian Li − *Department of Applied Chemistry, Graduate School of Engineering, Osaka University, Suita, Osaka 565-0871, Japan*

Ryosuke Nishikubo − *Department of Applied Chemistry, Graduate School of Engineering, Osaka University, Suita, Osaka 565-0871, Japan; Innovative Catalysis Science Division (ICS), Institute for Open and Transdisciplinary Research Initiatives (OTRI), Osaka University, Suita, Osaka 565-0871, Japan;* orcid.org/0000-0002-0533-9180

Complete contact information is available at: https://pubs.acs.org/10.1021/acsomega.3c09977

Notes

The authors declare no competing financial interest.

■ ACKNOWLEDGMENTS

We acknowledge the financial support received from KAKENHI of the Japan Society for the Promotion of Science (JSPS) (JP20H05836 and JP20H00398 to A.S.), the Japan Science and Technology Agency (JST) MIRAI (JPMJMI22E2 to A.S.), and the New Energy and Industrial Technology Development Organization (NEDO) Green Innovation Project (JP21578854 to A.S.).

■ REFERENCES

(1) Han, C.; Wang, J.; Zhang, S.; Chen, L.; Bi, F.; Wang, J.; Yang, C.; Wang, P.; Li, Y.; Bao, X. Over 19% Efficiency Organic Solar Cells by

Regulating Multidimensional Intermolecular Interactions. *Adv. Mater.* **2023**, *35*, 2208986.
(2) Zhu, L.; Zhang, M.; Xu, J.; Li, C.; Yan, J.; Zhou, G.; Zhong, W.; Hao, T.; Song, J.; Xue, X.; Zhou, Z.; Zeng, R.; Zhu, H.; Chen, C.-C.; MacKenzie, R. C. I.; Zou, Y.; Nelson, J.; Zhang, Y.; Sun, Y.; Liu, F. Single-Junction Organic Solar Cells with Over 19% Efficiency Enabled by a Refined Double-Fibril Network Morphology. *Nat. Mater.* **2022**, *21*, 656−663.
(3) Li, D.; Deng, N.; Fu, Y.; Guo, C.; Zhou, B.; Wang, L.; Zhou, J.; Liu, D.; Li, W.; Wang, K.; Sun, Y.; Wang, T. Fibrillization of Non-Fullerene Acceptors Enables 19% Efficiency Pseudo-Bulk Heterojunction Organic Solar Cells. *Adv. Mater.* **2023**, *35*, No. e2208211.
(4) Wang, Y.; Fan, Q.; Guo, X.; Li, W.; Guo, B.; Su, W.; Ou, X.; Zhang, M. High-Performance Nonfullerene Polymer Solar Cells Based on a Fluorinated Wide Bandgap Copolymer with a High Open-Circuit Voltage Of 1.04 V. *J. Mater. Chem. A* **2017**, *5*, 22180.
(5) Aldrich, T. J.; Matta, M.; Zhu, W.; Swick, S. M.; Stern, C. L.; Schatz, G. C.; Facchetti, A.; Melkonyan, F. S.; Marks, T. J. Fluorination Effects on Indacenodithienothiophene Acceptor Packing and Electronic Structure, End-Group Redistribution, and Solar Cell Photovoltaic Response. *J. Am. Chem. Soc.* **2019**, *141*, 3274−3287.
(6) Yuan, J.; Zhang, Y.; Zhou, L.; Zhang, G.; Yip, H.-L.; Lau, T.-K.; Lu, X.; Zhu, C.; Peng, H.; Johnson, P. A.; Leclerc, M.; Cao, Y.; Ulanski, J.; Li, Y.; Zou, Y. Single-Junction Organic Solar Cell with Over 15% Efficiency Using Fused-Ring Acceptor with Electron-Deficient Core. *Joule* **2019**, *3*, 1140−1151.
(7) Li, C.; Zhou, J.; Song, J.; Xu, J.; Zhang, H.; Zhang, X.; Guo, J.; Zhu, L.; Wei, D.; Han, G.; Min, J.; Zhang, Y.; Xie, Z.; Yi, Y.; Yan, H.; Gao, F.; Liu, F.; Sun, Y. Non-Fullerene Acceptors with Branched Side Chains and Improved Molecular Packing to Exceed 18% Efficiency in Organic Solar Cells. *Nat. Energy* **2021**, *6*, 605−613.
(8) Würfel, U.; Neher, D.; Spies, A.; Albrecht, S. Impact of Charge Transport on Current−Voltage Characteristics and Power-Conversion Efficiency of Organic Solar Cells. *Nat. Commun.* **2015**, *6*, 6951.
(9) Heiber, M. C.; Okubo, T.; Ko, S.-J.; Luginbuhl, B. R.; Ran, N. A.; Wang, M.; Wang, H.; Uddin, M. A.; Woo, H. Y.; Bazan, G. C.; Nguyen, T.-Q. Measuring the Competition between Bimolecular Charge Recombination and Charge Transport in Organic Solar Cells under Operating Conditions. *Energy Environ. Sci.* **2018**, *11*, 3019−3032.
(10) Firdaus, Y.; Corre, V. M. L.; Khan, J. I.; Kan, Z.; Laquai, F.; Beaujuge, P. M.; Anthopoulos, T. D. Key Parameters Requirements for Non-Fullerene-Based Organic Solar Cells with Power Conversion Efficiency> 20%. *Adv.Sci.* **2019**, *6*, 1802028.
(11) Zhao, F.; Zhang, H.; Zhang, R.; Yuan, J.; He, D.; Zou, Y.; Gao, F. Emerging Approaches in Enhancing the Efficiency and Stability in Non-Fullerene Organic Solar Cells. *Adv. Energy Mater.* **2020**, *10*, 2002746.
(12) Vithanage, D. A.; DevižDevižIs, A.; Abramavičius, V.; Infahsaeng, Y.; Abramavičius, D.; MacKenzie, R. C. I.; Keivanidis, P. E.; Yartsev, A.; Hertel, D.; Nelson, J.; Sundström, V.; Gulbinas, V. Visualizing Charge Separation in Bulk Heterojunction Organic Solar Cells. *Nat. Commun.* **2013**, *4*, 2334.
(13) Göhler, C.; Wagenpfahl, A.; Deibel, C. Nongeminate Recombination in Organic Solar Cells. *Adv. Electron. Mater.* **2018**, *4*, 1700505.
(14) Bartesaghi, D.; Pérez, I. D. C.; Kniepert, J.; Roland, S.; Turbiez, M.; Neher, D.; Koster, L. J. A. Competition between Recombination and Extraction of Free Charges Determines the Fill Factor of Organic Solar Cells. *Nat. Commun.* **2015**, *6*, 7083.
(15) Seo, S.; Sun, C.; Lee, J.-W.; Lee, S.; Lee, D.; Wang, C.; Phan, T. N.-L.; Kim, G.-U.; Cho, S.; Kim, Y.-H.; Kim, B. J. Importance of High-Electron Mobility in Polymer Acceptors for Efficient All-Polymer Solar Cells: Combined Engineering of Backbone Building Unit and Regioregularity. *Adv. Funct. Mater.* **2022**, *32*, 2108508.
(16) Zhang, G.; Xia, R.; Chen, Z.; Xiao, J.; Zhao, X.; Liu, S.; Yip, H.-L.; Cao, Y. Overcoming Space-Charge Effect for Efficient Thick-Film Non-Fullerene Organic Solar Cells. *Adv. Energy Mater.* **2018**, *8*, 1801609.
(17) Dong, X.; Jiang, Y.; Sun, L.; Qin, F.; Zhou, X.; Lu, X.; Wang, W.; Zhou, Y. Large-Area Organic Solar Modules with Efficiency Over 14%. *Adv. Funct. Mater.* **2022**, *32*, 2110209.
(18) Melianas, A.; Kemerink, M. Photogenerated Charge Transport in Organic Electronic Materials: Experiments Confirmed by Simulations. *Adv. Mater.* **2019**, *31*, No. e1806004.
(19) Schauer, F. Space-Charge-Limited Currents for Organic Solar Cells Optimisation. *Sol. Energy Mater. Sol. Cells* **2005**, *87*, 235−250.
(20) Choulis, S. A.; Nelson, J.; Kim, Y.; Poplavskyy, D.; Kreouzis, T.; Durrant, J. R.; Bradley, D. D. C. Investigation of Transport Properties in Polymer/Fullerene Blends Using Time-of-Flight Photocurrent Measurements. *Appl. Phys. Lett.* **2003**, *83*, 3812.
(21) Babel, A.; Jenekhe, S. A. Alkyl Chain Length Dependence of the Field-Effect Carrier Mobility in Regioregular Poly(3-Alkylthiophene)-s. *Synth. Met.* **2005**, *148*, 169.
(22) Juška, G.; Arlauskas, K.; Viliūnas, M.; Kočka, J. Extraction Current Transients: New Method of Study of Charge Transport in Microcrystalline Silicon. *Phys. Rev. Lett.* **2000**, *84*, 4946−4949.
(23) Juška, G.; NekrašNekrašAs, N.; Valentinavičius, V.; Meredith, P.; Pivrikas, A. Extraction of photogenerated charge carriers by linearly increasing voltage in the case of Langevin recombination. *Phys. Rev. B* **2011**, *84*, 155202.
(24) Katagiri, C.; Yoshida, T.; White, M. S.; Yumusak, C.; Sariciftci, N. S.; Nakayama, K.-I. Application of MIS-CELIV Technique to Measure Hole Mobility of Hole-Transport Material for Organic Light-Emitting Diodes. *AIP Adv.* **2018**, *8*, 105001.
(25) Pranculis, V.; Ruseckas, A.; Vithanage, D. A.; Hedley, G. J.; Samuel, I. D. W.; Gulbinas, V. Influence of Blend Ratio and Processing Additive on Free Carrier Yield and Mobility in PTB7: $PC_{71}BM$ Photovoltaic Solar Cells. *J. Phys. Chem. C* **2016**, *120*, 9588−9594.
(26) Ulbricht, R.; Hendry, E.; Shan, J.; Heinz, T. F.; Bonn, M. Carrier Dynamics in Semiconductors Studied with Time-Resolved Terahertz Spectroscopy. *Rev. Mod. Phys.* **2011**, *83*, 543.
(27) Saeki, A.; Yoshikawa, S.; Tsuji, M.; Koizumi, Y.; Ide, M.; Vijayakumar, C.; Seki, S. A Versatile Approach to Organic Photovoltaics Evaluation Using White Light Pulse and Microwave Conductivity. *J. Am. Chem. Soc.* **2012**, *134*, 19035−19042.
(28) Hamada, F.; Saeki, A. Mobility Relaxation of Holes and Electrons in Polymer: Fullerene and Polymer: Non-Fullerene Acceptor Solar Cells. *ChemSuschem* **2021**, *14*, 3528−3535.
(29) Melianas, A.; Etzold, F.; Savenije, T. J.; Laquai, F.; Inganäs, O.; Kemerink, M. Photo-Generated Carriers Lose Energy During Extraction from Polymer-Fullerene Solar Cells. *Nat. Commun.* **2015**, *6*, 8778.
(30) Schleuning, M.; Kölbach, M.; Abdi, F. F.; Schwarzburg, K.; Stolterfoht, M.; Eichberger, R.; van de Krol, R.; Friedrich, D.; Hempel, H. Generalized Method to Extract Carrier Diffusion Length from Photoconductivity Transients: Cases of $BiVO_4$, Halide Perovskites, and Amorphous and Crystalline Silicon. *PRX Energy* **2022**, *1*, 023008.
(31) Li, S.; Hamada, F.; Nishikubo, R.; Saeki, A. Quantifying the Optimal Thickness in Polymer: Fullerene Solar Cells from the Analysis of Charge Transport Dynamics and Photoabsorption. *Sustainable Energy Fuels* **2022**, *6*, 756−765.
(32) Savenije, T. J.; Ferguson, A. J.; Kopidakis, N.; Rumbles, G. Revealing the Dynamics of Charge Carriers in Polymer: Fullerene Blends Using Photoinduced Time-Resolved Microwave Conductivity. *J. Phys. Chem. C* **2013**, *117*, 24085−24103.
(33) Kumano, M.; Ide, M.; Seiki, N.; Shoji, Y.; Fukushima, T.; Saeki, A. A Ternary Blend of a Polymer, Fullerene, and Insulating Self-Assembling Triptycene Molecules for Organic Photovoltaics. *J. Mater. Chem. A* **2016**, *4*, 18490.
(34) Shimata, Y.; Saeki, A. Hole Relaxation in Polymer: Fullerene Solar Cells Examined by the Simultaneous Measurement of Time-of-Flight and Time-Resolved Microwave Conductivity. *J. Phys. Chem. C* **2017**, *121*, 18351−18359.
(35) Cheung, C. H.; Kwok, K. C.; Tse, S. C.; So, S. K. Determination of Carrier Mobility in Phenylamine by Time-of-Flight,

https://doi.org/10.1021/acsomega.3c09977
ACS Omega 2024, 9, 26951−26962

Dark-Injection, and Thin Film Transistor Techniques. *J. Appl. Phys.* **2008**, *103*, 093705.
(36) Osterbacka, R.; Pivrikas, A.; Juska, G.; Genevicius, K.; Arlauskas, K.; Stubb, H. Mobility and Density Relaxation of Photogenerated Charge Carriers in Organic Materials. *Curr. Appl. Phys.* **2004**, *4*, 534−538.
(37) Yan, L.; Wang, Y.; Wei, J.; Ji, G.; Gu, H.; Li, Z.; Zhang, J.; Luo, Q.; Wang, Z.; Liu, X.; Xu, B.; Wei, Z.; Ma, C.-Q. Simultaneous Performance and Stability Improvement of Polymer: Fullerene Solar Cells by Doping with Piperazine. *J. Mater. Chem. A* **2019**, *7*, 7099.
(38) Armin, A.; Juska, G.; Ullah, M.; Velusamy, M.; Burn, P. L.; Meredith, P.; Pivrikas, A. Balanced Carrier Mobilities: Not a Necessary Condition for High-Efficiency Thin Organic Solar Cells as Determined by MIS-CELIV. *Adv. Energy Mater.* **2014**, *4*, 1300954.
(39) Gao, M.; Burn, P. L.; Pivrikas, A. Balanced Hole and Electron Transport in $Ir(ppy)_3$: TCTA Blends. *ACS Photonics* **2021**, *8*, 2425−2430.
(40) Genevičius, K.; Österbacka, R.; Juška, G.; Arlauskas, K.; Stubb, H. Separation of fast and slow transport in regiorandom poly (3-hexylthiophene). *Synth. Met.* **2003**, *137*, 1407−1408.
(41) Sandberg, O. J.; Nyman, M.; Dahlström, S.; Sandén, S.; Törngren, B.; Smått, J.-H.; Österbacka, R. On the validity of MIS-CELIV for mobility determination in organic thin-film devices. *Appl. Phys. Lett.* **2017**, *110*, 153504.
(42) Pivrikas, A.; Sariciftci, N. S.; Juška, G.; Sterbacka, R. Ö. A Review of Charge Transport and Recombination in Polymer/Fullerene Organic Solar Cells. *Prog. Photovolt: Res. Appl.* **2007**, *15*, 677−696.
(43) Guo, Q.; Guo, Q.; Geng, Y.; Tang, A.; Zhang, M.; Du, M.; Sun, X.; Zhou, E. Recent Advances in PM6: Y6-Based Organic Solar Cells. *Mater. Chem. Front.* **2021**, *5*, 3257.
(44) De Haas, M. P.; Warman, J. M. Photon-Induced Molecular Charge Separation Studied by Nanosecond Time-Resolved Microwave Conductivity. *Chemiul Phy.* **1982**, *73*, 35−53.
(45) Infelta, P. P.; De Haas, M. P.; Warman, J. M. The Study of the Transient Conductivity of Pulse Irradiated Dielectric Liquids on a Nanosecond Timescale Using Microwaves. *Radiat. Phys. Chem.* **1977**, *10*, 353−365.
(46) Saeki, A.; Seki, S.; Koizumi, Y.; Tagawa, S. Dynamics of Photogenerated Charge Carrier and Morphology Dependence in Polythiophene Films Studied by in Situ Time-Resolved Microwave Conductivity and Transient Absorption Spectroscopy. *J. Photochem. Photobiol. A* **2007**, *186*, 158−165.
(47) Zhao, T.; Zhao, Q.; Lee, J.; Yang, S.; Wang, H.; Chuang, M.-Y.; He, Y.; Thompson, S. M.; Liu, G.; Oh, N.; Murray, C. B.; Kagan, C. R. Engineering the Surface Chemistry of Colloidal InP Quantum Dots for Charge Transport. *Chem. Mater.* **2022**, *34*, 8306−8315.
(48) Xu, Z.; Liu, Z.; Li, N.; Tang, G.; Zheng, G.; Zhu, C.; Chen, Y.; Wang, L.; Huang, Y.; Li, L.; Zhou, N.; Hong, J.; Chen, Q.; Zhou, H. A thermodynamically favored crystal orientation in mixed formamidinium/methylammonium perovskite for efficient solar cells. *Adv. Mater.* **2019**, *31*, No. e1900390.
(49) Tailor, N. K.; Yukta; Ranjan, R.; Ranjan, S.; Sharma, T.; Singh, A.; Garg, A.; Nalwa, K. S.; Gupta, R. K.; Satapathi, S. The effect of dimensionality on the charge carrier mobility of halide perovskites. *J. Mater. Chem. A* **2021**, *9*, 21551−21575.
(50) Zarifi, M. H.; Mohammadpour, A.; Farsinezhad, S.; Wiltshire, B. D.; Nosrati, M.; Askar, A. M.; Daneshmand, M.; Shankar, K. Time-Resolved Microwave Photoconductivity (TRMC) Using Planar Microwave Resonators: Application to The Study of Long-Lived Charge Pairs in Photoexcited Titania Nanotube Arrays. *J. Phys. Chem. C* **2015**, *119*, 14358−14365.
(51) Armin, A.; Juska, G.; Philippa, B. W.; Burn, P. L.; Meredith, P.; White, R. D.; Pivrikas, A. Doping-Induced Screening of the Built-in-Field in Organic Solar Cells: Effect on Charge Transport and Recombination. *Adv. Energy Mater.* **2013**, *3*, 321−327.
(52) Gao, M.; Burn, P. L.; Pivrikas, A. Charge Transport in an Organic Light Emitting Diode Material Measured Using Metal-Insulator-Semiconductor Charge Extraction by Linearly Increasing Voltage with Parameter Variation. *J. Appl. Phys.* **2019**, *126*, 035501.
(53) Neukom, M. T.; Reinke, N. A.; Ruhstaller, B. Charge Extraction with Linearly Increasing Voltage: a Numerical Model for Parameter Extraction. *Sol. Energy* **2011**, *85*, 1250−1256.
(54) Katagiri, C.; Nakayama, K.-I. Effect of built-in potential on charge carrier mobility evaluated from extraction current transients in poly (3-hexylthiophene) thin film. *Appl. Phys. Express* **2018**, *11*, 011601.
(55) Suzuki, Y.; Adachi, S.; Suenobu, T.; Suzuki, M.; Nakayama, K.-I. Effect of the MIS structure with MgF2 on CELIV measurements. *Jpn. J. Appl. Phys.* **2020**, *59*, SDDB01.
(56) Gon, H. B.; Veeraiah, N. Dielectric properties of LiF single crystals. *J. Mater. Sci.* **1981**, *16*, 2571−2574.
(57) Laquai, F.; Andrienko, D.; Mauer, R.; Blom, P. W. M. Charge carrier transport and photogeneration in P3HT: PCBM photovoltaic blends. *Macromol. Rapid Commun.* **2015**, *36*, 1001−1025.
(58) Duan, L.; Zhang, Y.; Yi, H.; Haque, F.; Xu, C.; Wang, S.; Uddin, A. Thermal annealing dependent dielectric properties and energetic disorder in PffBT4T-2OD based organic solar cells. *Mater. Sci. Semicond.* **2020**, *105*, 104750.
(59) Li, P.; Fang, J.; Wang, Y.; Manzhos, S.; Cai, L.; Song, Z.; Li, Y.; Song, T.; Wang, X.; Guo, X.; Zhang, M.; Ma, D.; Sun, B. Synergistic effect of dielectric property and energy transfer on charge separation in non-fullerene-based solar cells. *Angew. Chem., Int. Ed.* **2021**, *60*, 15054−15062.
(60) Melianas, A.; Pranculis, V.; Xia, Y.; Felekidis, N.; Inganäs, O.; Gulbinas, V.; Kemerink, M. Photogenerated Carrier Mobility Significantly Exceeds Injected Carrier Mobility in Organic Solar Cells. *Adv. Energy Mater.* **2017**, *7*, 1602143.
(61) Juška, G.; Nekrašas, N.; Genevičius, K. Investigation of charge carriers transport from extraction current transients of injected charge carriers. *J. Non-Cryst. Solids* **2012**, *358*, 748−750.
(62) Heiber, M. C.; Herzing, A. A.; Richter, L. J.; DeLongchamp, D. M. Charge Transport and Mobility Relaxation in Organic Bulk Heterojunction Morphologies Derived from Electron Tomography Measurements. *J. Mater. Chem. C* **2020**, *8*, 15339.
(63) Schubert, M.; Preis, E.; Blakesley, J. C.; Pingel, P.; Scherf, U.; Neher, D. Mobility Relaxation and Electron Trapping in a Donor/Acceptor Copolymer. *Phys. Rev. B* **2013**, *87*, 024203.
(64) Philippa, B.; Stolterfoht, M.; Burn, P. L.; Juška, G.; Meredith, P.; White, R. D.; Pivrikas, A. The Impact of Hot Charge Carrier Mobility on Photocurrent Losses in Polymer-Based Solar Cells. *Sci. Rep.* **2014**, *4*, 5695.
(65) Philippa, B.; Vijila, C.; White, R. D.; Sonar, P.; Burn, P. L.; Meredith, P.; Pivrikas, A. Time-Independent Charge Carrier Mobility in a Model Polymer: Fullerene Organic Solar Cell. *Org. Electron.* **2015**, *16*, 205−211.
(66) Zhou, J.; Zhou, Y. C.; Zhao, J. M.; Wu, C. Q.; Ding, X. M.; Hou, X. Y. Carrier Density Dependence of Mobility in Organic Solids: A Monte Carlo Simulation. *Phys. Rev. B* **2007**, *75*, 153201.
(67) Juška, G.; Arlauskas, K.; Viliūnas, M.; Genevičius, K.; Österbacka, R.; Stubb, H. Charge transport in π-conjugated polymers from extraction current transients. *Phys. Rev. B* **2000**, *62*, R16235.
(68) Tokmoldin, N.; Hosseini, S. M.; Raoufi, M.; Phuong, L. Q.; Sandberg, O. J.; Guan, H.; Zou, Y.; Neher, D.; Shoaee, S. Extraordinarily long diffusion length in PM6: Y6 organic solar cells. *J. Mater. Chem. A* **2020**, *8*, 7854−7860.
(69) Oh, J.; Lee, S. M.; Jung, S.; Lee, J.; Park, G.; Kang, S.-H.; Cho, Y.; Jeong, M.; Lee, B.; Kim, S.; Yan, C. Antioxidant Additive with a High Dielectric Constant for High Photo-Oxidative Stabilization of Organic Solar Cells without Almost Sacrificing Initial High Efficiencies. *Sol. RRL* **2021**, *5*, 2000812.
(70) Perdigón-Toro, L.; Zhang, H.; Markina, A.; Yuan, J.; Hosseini, S. M.; Wolff, C. M.; Zuo, G.; Stolterfoht, M.; Zou, Y.; Gao, F.; Andrienko, D.; Shoaee, S.; Neher, D. Barrierless Free Charge Generation in the High-Performance PM6: Y6 Bulk Heterojunction Non-Fullerene Solar Cell. *Adv. Mater.* **2020**, *32*, No. e1906763.

https://doi.org/10.1021/acsomega.3c09977
ACS Omega 2024, 9, 26951−26962